Azimuthal Anisotropy at Valhall: the Helmholtz Equation Approach

Aurélien Mordret,[1] Nikolaï M. Shapiro[1], Satish Singh[2], Philippe Roux[3],

Jean-Paul Montagner[1], Olav. I. Barkved[4]

A. Mordret, Institut de Physique du Globe de Paris, 1 rue Jussieu 75005, Paris, France. (mordret@ipgp.fr)

N. M. Shapiro, Institut de Physique du Globe de Paris, 1, rue Jussieu - 75238 Paris cedex 05 , France. (nshapiro@ipgp.fr)

S. C. Singh, Institut de Physique du Globe de Paris, 1, rue Jussieu - 75238 Paris cedex 05 , France. (singh@ipgp.fr)

P. Roux, ISTerre, 1381 rue de la Piscine BP 53, 38041 Grenoble CEDEX 9, France. (philippe.roux@obs.ujf-grenoble.fr)

J. P. Montagner, Institut de Physique du Globe de Paris, 1, rue Jussieu - 75238 Paris cedex 05, France. (jpm@ipgp.fr)

O. I. Barkved , BP Norge AS, P.O. Box 197, 4065 Stavanger, Norway. (olav-inge.barkved@no.bp.com)

[1]Institut de Physique du Globe de Paris,

France. Laboratoire de sismologie

We used 6 hours of continuous vertical records from 2320 sensors of the Valhall *Life of Fields Seismic* network to compute 2 690 040 cross-correlation functions between the full set of sensor pair combinations. We applied the 'Helmholtz tomography' approach combined with the ambient noise correlation method to track the wave front across the network with every station considered as a virtual source. The gradient of the interpolated phase travel time gives us an estimate of the local phase speed and of the direction of wave propagation. By combining the individual measurements for every station, we estimated the distribution of Scholte's wave phase speeds with respect to azimuth. The observed cosine pattern indicates the presence of azimuthal anisotropy. The elliptic shape of the fast anisotropy direction is consistent with results of previous shear wave splitting studies and reflects the strong seafloor subsidence due to the hydrocarbon reservoir depletion at depth and is in good agreement with geomechanical modeling.

[2]Institut de Physique du Globe de Paris,

France. Laboratoire de geosciences marines

[3]ISTerre, Grenoble, France

[4]BP, Stavanger, Norway

1. Introduction

Seismic anisotropy information is complementary to that of isotropic velocity and is becoming more and more important in exploration and engineering seismology [e.g., *Tsvankin et al.*, 2010]. Many studies about azimuthal anisotropy were carried out by analyzing the shear-wave splitting (SWS) of compressional waves converted at different interfaces. However, depending on the depth of the interface where P-waves are converted, the measured anisotropy integrates the varying anisotropy along the whole ray path and it may be difficult to infer its depth distribution properly. Surface-wave dispersion (the larger the period, the deeper the surface-wave sensitivity) and the fact that they travel horizontally along the Earth surface allow us to retrieve the 3D distribution of anisotropy using this type of waves. The azimuthal anisotropy at the global and regional scales is often retrieved from surface-waves emitted by earthquakes [e.g. *Montagner and Nataf*, 1986; *Montagner and Tanimoto*, 1991; *Barmin et al.*, 2001; *Trampert and Woodhouse*, 2003; *Smith et al.*, 2004; *Ekström*, 2011].

Deterministic signals extracted from cross-correlations (CC's) of seismic noise [e.g., *Gouédard et al.*, 2008, and references therein] provide a very attractive alternative to earthquake or active sources. For receivers installed on the earth surface, these noise CCs are dominated by fundamental-mode surface waves [*Shapiro and Campillo*, 2004]. This technique of noise-based surface-wave imaging methods developed very rapidly during recent years. It is particularly advantageous within the context of modern seismic arrays where computing the CCs between all pairs of sensors results in very dense and azimuthally well distributed path coverage. Noise-based surface wave imaging has been applied at

regional and continental scales to infer isotropic [e.g., *Shapiro et al.*, 2005; *Yao et al.*, 2006; *Yang et al.*, 2008; *Stehly et al.*, 2009] and anisotropic [e.g., *Lin et al.*, 2009; *Fry et al.*, 2010; *Lin et al.*, 2010, 2011] structures. *Durand et al.* [2011] used polarization analysis of surface waves retrieved from cross-correlations to infer temporal changes of anisotropy related to the 2004 Parkfield earthquake.

The noise correlation approach has also been applied to continuous records from industrial seismic networks to extract reflection response [*Draganov et al.*, 2007] and surface waves [*Mordret et al.*, 2012a] . In the present paper, we use the data of the Valhall *Life of Fields Seismic* network (*LoFS*, Fig. 1) to extract Scholte waves (i.e., interface waves traveling between a water layer and the subsurface) from cross-correlation of ambient seismic noise, and to determine azimuthal anisotropy in the shallow subsurface at a kilometric scale. The Valhall *LoFS* network operated by BP Norge A/S was installed on the North Sea seafloor in 2003 over the Valhall oil field. The network covers 70% of the field area and is made of 120 km of ocean bottom cables buried at 1 m depth in the soil where data are continuously recorded by 2320 4-component seismic sensors (4C: Up, North, East and Hydrophone)[e.g., *VanGestel et al.*, 2008; *de Ridder and Dellinger*, 2011; *Mordret et al.*, 2012a]. After computing the CCs between all pairs of sensors, we use the 'Helmholtz' technique of *Lin and Ritzwoller* [2011a] to infer the variations of the surface wave speed with respect to the azimuth and to determine azimuthal anisotropy with a straightforward method not requiring a formal tomographic inversion.

2. Data and noise cross-correlations

We analyzed ∼6.5 hours (400 min) of continuous signals recorded at 250 Hz from 2320 sensors of the *LoFS* network. The CCs computation is described in detail by *Mordret et al.* [2012a] and partly follows the workflow of *Bensen et al.* [2007], involving spectral whitening between 0.5 and 2.85 s before computing the CCs. Because the data do not present strong amplitude variations, we did not used temporal normalization. In this study, we focused on Scholte waves and used the ZZ cross-correlations from 2 690 040 station pairs.

Mordret et al. [2012a] showed that the ambient noise recorded during the considered six hours is strongly affected by two operating platforms: one in the center of the network and another one at the south (Fig. 1). The noise source distribution was found homogeneous only for the 0.5 - 2.85 s period band, where the CCs were symmetric. At shorter period, the exploitation platforms act as a strongly dominant localized noise point source preventing the convergence of the CCs toward Green functions for most of the station pairs. Therefore, we only analyze here the CCs above 0.5 s that contain reconstructed Scholte waves.

3. Method

We consider every station i as a virtual source recorded by all other stations. We illustrate the processing with one virtual source (station 371, Fig. 1) that is repeated for all 2319 stations. We treat the CCs as virtual seismograms and use them to measure phase travel times $\tau_i(\mathbf{r}, \omega)$ where $\mathbf{r}$ is the position and ω is the angular frequency. Following the approach of *Lin and Ritzwoller* [2011a] and *Mordret et al.* [2012b], we use the the frequency

dependent Eikonal equation derived from the 2D Helmholtz wave equation [*Biondi*, 1992] to compute phase speeds $c(\mathbf{r})$:

$$\frac{1}{c_i(\mathbf{r})^2} = |\nabla \tau_i(\mathbf{r})|^2 - \frac{\Delta A_i(\mathbf{r})}{A_i(\mathbf{r})\omega^2}, \quad (1)$$

where A is the the spectral amplitude at frequency ω. The symbols ∇ and Δ stand for the gradient and the Laplacian, respectively. As a result, at every position $\mathbf{r}$ we obtain a set of local phase speeds and a set of local wave propagation directions (taken as the gradient direction) measured for every virtual source i. We then study the dependence of this phase speed on the local wave propagation direction ψ to evaluate the different Fourier series expansion of the azimuthal anisotropy in azimuth ψ, taken positive clockwise with respect to North.

3.1. Helmholtz tomography

Our approach of Helmholtz tomography is described in details by *Mordret et al.* [2012b]. We briefly summarise here main steps highlighting when there are differences from *Mordret et al.* [2012b]. Fig. 2 shows an example of symmetric CCs computed for one reference station (station 371, see Fig. 1) and arranged with increasing inter-station distance. We first perform a waveform selection similar to *Mordret et al.* [2012b], rejecting symmetric CCs between 0.5 and 2.85 s which have a signal-to-noise ratio (SNR) lower than 3 (contrary to *Mordret et al.* [2012b] who keep signals with SNR above 1.5) in the move-out window defined by the black lines in Fig. 2. The white strips show the CCs that did not passed the selection criteria. Finally, we do not consider as virtual sources stations where after the selection there are less than 30 CCs and where the azimuthal coverage

of all selected paths to other stations is less than 180°. On average, we reject $\sim$ 55 % of the CCs based on the above criteria. We measure the phase travel-time using the equation of the spectral phases $\varphi(\omega)$ of a single-mode surface waves [*Mordret et al.*, 2012b]:

$$\varphi(\omega) = -\omega t + n \cdot 2\pi + \varphi_0, \tag{2}$$

where ω is the angular frequency, $n \cdot 2\pi$ is the intrinsic 2π phase ambiguity ($n \in$ Integer) and φ_0 is a real constant term containing the spatial propagation term and the initial source phase.

For every selected CC, we then compute the frequency dependent phase travel-time : $t_c(\omega)$ as

$$t_c(\omega) = \frac{-\varphi(\omega) + n \cdot 2\pi + \varphi_0}{\omega}, \tag{3}$$

We do not need to solve for the initial phase ambiguity because the constant term in Equation 3 cancel each other when computing travel-time gradients. At this stage, we also measured the spectral amplitudes $A(\omega)$ that are used in equation 1. To compute the gradient of the travel time and the Laplacian of the amplitude, we interpolate the phase travel times and the amplitude onto a regular grid (see Supplementary material, Fig. S1) following *Mordret et al.* [2012b].

Computing the right-hand term of Equation 1 for every virtual source results in a set of vectors whose directions characterize the local wave propagation direction and and whose amplitudes are equal to local phase slownesses. The inset in Fig. 3 shows a set of three vectors, associated with one cell of the model, in which the local phase velocity

and local direction of wave propagation are inferred from three different virtual sources. Depending on its location in the model (at the periphery or in the center of the network) each cell is spanned by the measurements from 0 up to ∼300 virtual sources. We used the inferred relationship between the local phase velocities and local directions of propagation to compute the azimuthal anisotropy at each point of the grid.

3.2. Parameterization of the azimuthal anisotropy

Smith and Dahlen [1973] showed that for a slightly anisotropic medium at any given frequency, the surface-wave phase velocity relationship with the azimuth ψ is in the form of an even order sinusoid with 180°and 90°periodicity. Similarly to *Lin and Ritzwoller* [2011a], we find that overlaying the usual 2ψ and 4ψ component, there is also sometimes a 360°periodicity or 1ψ component. We thus chose the following functional form to fit our phase velocity measurements with respect to the azimuth:

$$c(\psi) = c_0 + \frac{A'}{2c_0}\cos(1(\psi - \phi_1)) + \frac{B'}{2c_0}\cos(2(\psi - \phi_2)) + \frac{C'}{2c_0}\cos(3(\psi - \phi_3)) + \frac{D'}{2c_0}\cos(4(\psi - \phi_4)). \tag{4}$$

Equation 4 represents a truncated Fourier series analysis of our data. Here c_0 is the average phase velocity for one station, $A = A'/c_0$, $B = B'/c_0$, $C = C'/c_0$ and $D = D'/c_0$ are the peak-to-peak relative amplitude of the 1ψ, 2ψ, 3ψ and 4ψ terms and ϕ_1, ϕ_2, ϕ_3 and ϕ_4 define the orientation of the fast axes for the 1ψ, 2ψ, 3ψ and 4ψ terms, respectively.

Tu reduce uncertainties, we follow *Lin et al.* [2009] and combine together all measurements from a a 550 m × 550 m super-cell (11×11 cells). These combined measurements are represented by the small blue dots in Fig. 3. Then, we average the measurements in 20°azimuthal bins to retrieve the mean speeds and their standard deviations (large red

dots with error bars in Fig. 3). We fitted these final averaged measurements in a weighted least-square sense with Equation 4 and obtained the red curve in Fig. 3. We defined the misfit of our inversion at a single station as the standard deviation between the measured and the predicted phase speeds. We only keep for interpretation the stations with a misfit smaller than 15 m/s.

4. Results

Because in this study we have a similar data coverage as *Mordret et al.* [2012a] , we assume that the spatial resolution of our anisotropy measurements has the same order of magnitude, i.e. about 320 m at 0.7 s period. Thus, to have independent anisotropy measurements at 0.7 s, we inverted for the azimuthal anisotropy at every 6th station (every 300 m in the along cable direction). Fig. 4A shows the map of the fast axis and amplitude of the 2ψ anisotropy obtained at 0.7 s with the Helmholtz tomography approach. The 2ψ anisotropy exhibits an elliptic pattern roughly centered on the main exploitation platform with a high amplitude anisotropy ring about 2-3 km from the platform. Our data quality criterion selection removed all stations in a 1.5 km radius circle around the platform because of the low SNR of the CCs in this area [*Mordret et al.*, 2012a] and also some measurements on the western and eastern lines because the mesurements are less constrained on the edges of the network and because these regions are more heterogeneous with strong velocity gradients [*Mordret et al.*, 2012a] . We also observe in these parts significant 1ψ and 3ψ components (Supplementary material, Fig. S2) suggesting that they might be partially caused by a poor azimuthal coverage. On average, the amplitudes of

the 3ψ and 4ψ terms are about twice smaller than the 2ψ and 1ψ amplitudes (Fig. 3 and Supplementary material, Fig. S2-S3-S6) and we do not consider them in the following.

5. Discussion and Conclusion

The elliptic pattern of the 2ψ anisotropy at Valhall is well-known and is due to the production-induced subsidence of the seafloor [*Olofsson et al.*, 2003; *Zwartjes et al.*, 2008]. A similar pattern have been observed at another field [e.g. *Van Dok et al.*, 2003]. Geomechanical modelings done by *Herwanger and Horne* [2005, 2009]; *Hatchell et al.* [2009] showed that such a subsidence created a maximum principal horizontal stress that was tangential to the subsidence bowl.

Two different mechanisms may be considered to explain the observed 2ψ anisotropy elliptic pattern. First, the shallow overburden is roughly made of horizontal sediment layers which can be seen as a vertical-transverse isotropic (VTI) medium. Because of the subsidence, the VTI medium becomes tilted on the edge of the bowl which may produce the observed anisotropy. Second possible mechanism is the presence of concentric fractures created by the subsidence-induced strain on the shoulder of the subsidence bowl. Both mechanisms, would result in elliptic anisotropy pattern in top hundreds of meters below the surface, which is in very good agreement with our observations (0.7 s the Scholte waves are sensitive to a depth $\sim$100-150 m) as well as results from shear-wave splitting [*Olofsson et al.*, 2003; *Barkved et al.*, 2005; *Maultzsch et al.*, 2006; *Zwartjes et al.*, 2008].

5.1. Anisotropy from average phase velocities

To check the robustness of the obtained results, we measured the phase velocity variations with the azimuth with a different method. We started the analysis with the same

set of phase travel times for each station. By dividing the distances between the central station and the surrounding ones by the phase travel times between these stations and sorting these average phase velocities as a function of the azimuth (Fig. S5), we were able to retrieve a clear anisotropic pattern (Fig. 4B). The fit of these data with Equation 4 give results that are generally consistent with our previous method (Fig. S5). Because this method averages the velocity fluctuations along the straight ray between the virtual source and the stations, it results in a smoother circular shape and stronger 1ψ anisotropic signals (Fig. 4B and Supplementary material, Fig. S2-S3-S5). Although a-priori less accurate than using local gradients, this method is a good proxy for the azimuthal anisotropy measurements with very dense seismic networks.

5.2. 1ψ term

The 1ψ component has already been highlighted at larger scale in Western US by *Lin and Ritzwoller* [2011a, b] who argue that this feature is a systematic bias caused by finite frequency effects, particularly unmodelled backward scattering on sharp velocity contrasts near stations. In general, a 1ψ component indicates a strong velocity gradient at the location of the measurement. In our Helmholtz tomography approach, the large amplitude 1ψ anisotropy is seen along the edges of the network where the azimuthal coverage is poor (around 180°or less) and the number of available data smaller. We thus deduce that the 1ψ component is mainly caused by errors related to the unconstrained fitting (less than 360°coverage) of the phase velocities. In our second approach, the phase velocity measurements are averaged along the distance between the sensors (which can be up to 2 km). As a result, the sharp isotropic velocity contrasts are integrated in the

velocity measurements. The 1ψ anisotropy is then larger at stations located on strong velocity gradients and points from the slower structure to the faster [*Mordret et al.*, 2012a, and Supplementary material, Fig. S2].

5.3. Conclusion

We measured the exploration-induced anisotropy in a shallow seafloor by combining two approaches that appeared during recent years : (1) the passive noise-based interferometric methods and (2) the Helmholtz tomography applied to the data from a very dense seismic array. We would like to emphasize two aspects of this study. First, the methods we used are robust, straightforward and simple to implement because, beside the cosine fitting, they do not involve formal inversion. Second, we showed that only 6.5 hours of continuous vertical records were sufficient to retrieve the spatial distribution of the azimuthal anisotropy at the Valhall field. This paves the way for developing passive time-dependent measurements of changes in anisotropy in shallow subsurface either in context of exploration or for monitoring active geological objects.

Acknowledgments. We thank BP Norge AS and the Valhall partner, Hess Norge AS, for granting access to the seismic data. The authors also acknowledge the use of resources provided by the European Grid Infrastructure. For more information, please consult the EGI-InSPIRE paper (http://go.egi.eu/pdnon). We are grateful to William Frank for his critical readings of an early version of this paper. The contribution of AM, NS, and PR was supported by a FP7 ERC Advanced grant 227507 (WHISPER). This is IPGP contribution number 3389.

References

Barkved, O., T. Kristiansen, and E. Fjær (2005), The 4d seismic response of a compacting reservoir-examples from the valhall field, norway., in *2005 SEG Annual Meeting*.

Barmin, M., M. Ritzwoller, and A. Levshin (2001), A fast and reliable method for surface wave tomography, *Pure and Applied Geophysics*, *158*(8), 1351–1375.

Bensen, G., M. Ritzwoller, M. Barmin, A. Levshin, F. Lin, M. Moschetti, N. Shapiro, and Y. Yang (2007), Processing seismic ambient noise data to obtain reliable broad-band surface wave dispersion measurements, *Geophysical Journal International*, *169*(3), 1239–1260.

Biondi, B. (1992), Solving the frequency-dependent eikonal equation, in *1992 SEG Annual Meeting*.

de Ridder, S., and J. Dellinger (2011), Ambient seismic noise eikonal tomography for near-surface imaging at valhall, *The Leading Edge*, *30*(5), 506–512.

Draganov, D., K. Wapenaar, W. Mulder, J. Singer, and A. Verdel (2007), Retrieval of reflections from seismic background-noise measurements, *Geophysical Research Letters*, *34*(4), L04,305.

Durand, S., J. Montagner, P. Roux, F. Brenguier, R. Nadeau, and Y. Ricard (2011), Passive monitoring of anisotropy change associated with the parkfield 2004 earthquake, *Geophysical Research Letters*, *38*(13), L13,303.

Ekström, G. (2011), A global model of love and rayleigh surface wave dispersion and anisotropy, 25–250 s, *Geophysical Journal International*.

Fry, B., F. Deschamps, E. Kissling, L. Stehly, and D. Giardini (2010), Layered azimuthal anisotropy of rayleigh wave phase velocities in the european alpine lithosphere inferred from ambient noise, *Earth and Planetary Science Letters*, *297*(1), 95–102.

Gouédard, P., L. Stehly, F. Brenguier, M. Campillo, Y. Colin de Verdière, E. Larose, L. Margerin, P. Roux, F. Sánchez-Sesma, N. Shapiro, and R. Weaver (2008), Cross-correlation of random fields: mathematical approach and applications, *Geophysical prospecting*, *56*(3), 375–393.

Hatchell, P., P. Wills, and C. Didraga (2009), Production Induced Effects on Near-surface Wave Velocities at Valhall, in *71st EAGE Conference and Exhibition*.

Herwanger, J., and S. Horne (2005), Predicting time-lapse stress effects in seismic data, *The Leading Edge*, *24*(12), 1234–1242.

Herwanger, J. V., and S. A. Horne (2009), Linking reservoir geomechanics and time-lapse seismics: Predicting anisotropic velocity changes and seismic attributes, *Geophysics*, *74*(4), W13–W33.

Lin, F., and M. Ritzwoller (2011a), Helmholtz surface wave tomography for isotropic and azimuthally anisotropic structure, *Geophysical Journal International*, *186*, 1104–1120.

Lin, F., and M. Ritzwoller (2011b), Apparent anisotropy in inhomogeneous isotropic media, *Geophysical Journal International*, *1*, 202.

Lin, F., M. Ritzwoller, and R. Snieder (2009), Eikonal tomography: surface wave tomography by phase front tracking across a regional broad-band seismic array, *Geophysical Journal International*, *177*(3), 1091–1110.

Lin, F., M. Ritzwoller, Y. Yang, M. Moschetti, and M. Fouch (2010), Complex and variable crustal and uppermost mantle seismic anisotropy in the western united states, *Nature Geoscience*, *4*(1), 55–61.

Lin, F., M. Ritzwoller, Y. Yang, M. Moschetti, and M. Fouch (2011), Complex and variable crustal and uppermost mantle seismic anisotropy in the western united states, *Nature Geoscience*, *4*(1), 55–61.

Maultzsch, S., F. Mancini, and S. Payne (2006), Observations of time-lapse converted-wave anomalies on valhall lofs data, in *EAGE 68th Conference & Exhibition*.

Montagner, J., and H. Nataf (1986), A simple method for inverting the azimuthal anisotropy of surface waves, *Journal of Geophysical Research*, *91*(B1), 511–520.

Montagner, J., and T. Tanimoto (1991), Global upper mantle tomography of seismic velocities and anisotropies, *Journal of Geophysical Research*, *96*(B12), 20,337–20.

Mordret, A., M. Landès, N. M. Shapiro, S. Singh, P. Roux, and O. I. Barkved (2012a), Studying seabed above the Valhall oil field with Ambient Noise Surface Wave Tomography, *Geophysical Journal International, In Press*.

Mordret, A., N. M. Shapiro, S. Singh, P. Roux, and O. I. Barkved (2012b), Helmholtz Tomography of ambient noise surface wave data to estimate Scholte wave phase velocity at Valhall Life of the Field, *Geophysics, In Press*.

Olofsson, B., T. Probert, J. Kommedal, and O. Barkved (2003), Azimuthal anisotropy from the valhall 4c 3d survey, *The Leading Edge*, *22*(12), 1228.

Shapiro, N., and M. Campillo (2004), Emergence of broadband rayleigh waves from correlations of the ambient seismic noise, *Geophys. Res. Lett*, *31*(7), 1615–1619.

Shapiro, N., M. Campillo, L. Stehly, and M. Ritzwoller (2005), High-resolution surface-wave tomography from ambient seismic noise, *Science*, *307*(5715), 1615–1618.

Smith, D., M. Ritzwoller, and N. Shapiro (2004), Stratification of anisotropy in the pacific upper mantle, *J. geophys. Res*, *109*(10.1029).

Smith, M., and F. Dahlen (1973), The azimuthal dependence of love and rayleigh wave propagation in a slightly anisotropic medium, *Journal of Geophysical Research*, *78*(17), 3321–3333.

Stehly, L., B. Fry, M. Campillo, N. Shapiro, J. Guilbert, L. Boschi, and D. Giardini (2009), Tomography of the alpine region from observations of seismic ambient noise, *Geophysical Journal International*, *178*(1), 338–350.

Trampert, J., and J. Woodhouse (2003), Global anisotropic phase velocity maps for fundamental mode surface waves between 40 and 150 s, *Geophysical Journal International*, *154*(1), 154–165.

Tsvankin, I., J. Gaiser, V. Grechka, M. van der Baan, and L. Thomsen (2010), Seismic anisotropy in exploration and reservoir characterization: An overview, *Geophysics*, *75*(5), 75A15.

Van Dok, R. R., J. E. Gaiser, and G. Byerley (2003), Near-surface shear-wave birefringence in the north sea: Ekofisk 2d/4c test, *The Leading Edge*, *22*(12), 1236–1242.

VanGestel, J.-P., J. H. Kommedal, O. I. Barkved, I. Mundal, R. Bakke, and K. D. Best (2008), Continuous seismic surveillance of Valhall Field, *The Leading Edge*, *27*(12), 1616–1621, doi:DOI: 10.1190/1.3036964.

Yang, Y., M. Ritzwoller, F. Lin, M. Moschetti, and N. Shapiro (2008), Structure of the crust and uppermost mantle beneath the western united states revealed by ambient noise and earthquake tomography, *J. geophys. Res*, *113*, B12,310.

Yao, H., R. Van Der Hilst, and M. De Hoop (2006), Surface-wave array tomography in se tibet from ambient seismic noise and two-station analysis–i. phase velocity maps, *Geophysical Journal International*, *166*(2), 732–744.

Zwartjes, P., P. Wills, J. De Maag, and P. Hatchell (2008), Shallow and Deep Time-lapse Effects on Valhall LoFS Converted Wave Data, in *70th EAGE Conference and Exhibition - Rome, Italy*.

Figure 1. Map of the Valhall *LoFS* network. Each dot is a 4C sensor. The distance between the sensors is 50 m and is 300 m between the lines. The black star shows the position of the station 371 used in Fig. 2 and 3, the black dot shows the station 1390 used in the Supplementary Materials. The circles show the approximate positions of the exploitation platforms. In the inset, the location of the Valhall field is shown by the red star.

Figure 2. Symmetric CCs between station 371 and every surrounding stations in a 10 wavelengths radius (at 0.7 s) sorted with respect to the distance between the stations and filtered between 0.67 and 2.85 s. The solid black lines show the window move-out where the signal is analyzed. The black dots are the phase travel time picks at 0.7 s that passed the quality criterion steps. The black dashed lines stand for 2 and 6 wavelengths where the travel times are kept.

Figure 3. Azimuthal distribution of the phase velocity at 0.7 s for the cell containing station 371. The small blue dots are the phase velocity measurements. The large red dots with error bars are the phase velocity averaged over 20°. The thick red curve is the best fits for the 1ψ, 2ψ, 3ψ and 4ψ azimuthal variation for the averaged velocity measurements. The values of the fitted parameters are shown. The inset shows a schematic diagram that illustrates the anisotropy measurements (vectors $\mathbf{C}(C, \psi)$ with C the phase velocity as magnitude and ψ the azimuth of propagation as the vector direction) at one cell of the model (small black square) related to 3 surrounding stations or virtual sources (colored triangles). Each colored vector field shows the velocity field of the waves emitted by the corresponding colored virtual source (see Supplementary material). The vectors in the particular cell are enlarged for clarity.

Figure 4. A) 2ψ azimuthal anisotropy fast direction and amplitude map at 0.7 s measured with the Helmholtz equation. B) 2ψ azimuthal anisotropy fast direction and amplitude map at 0.7 s measured with average phase velocities.

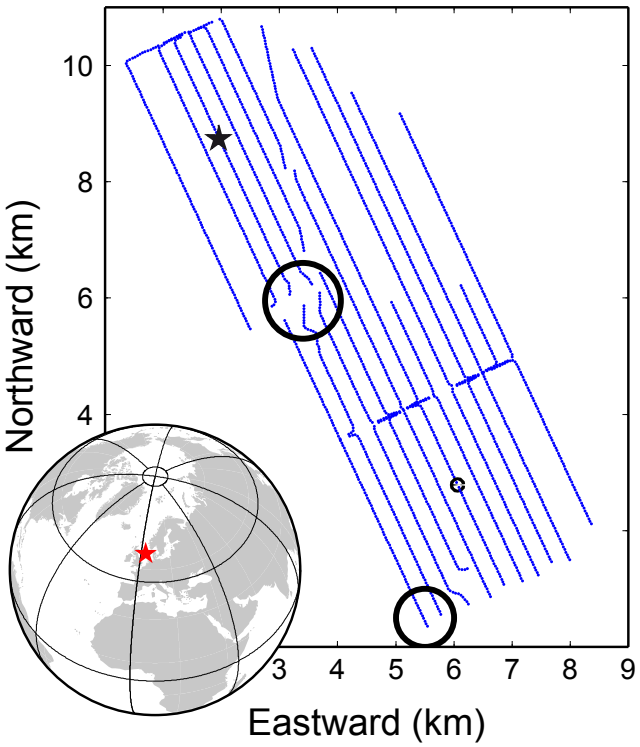

Figure 1

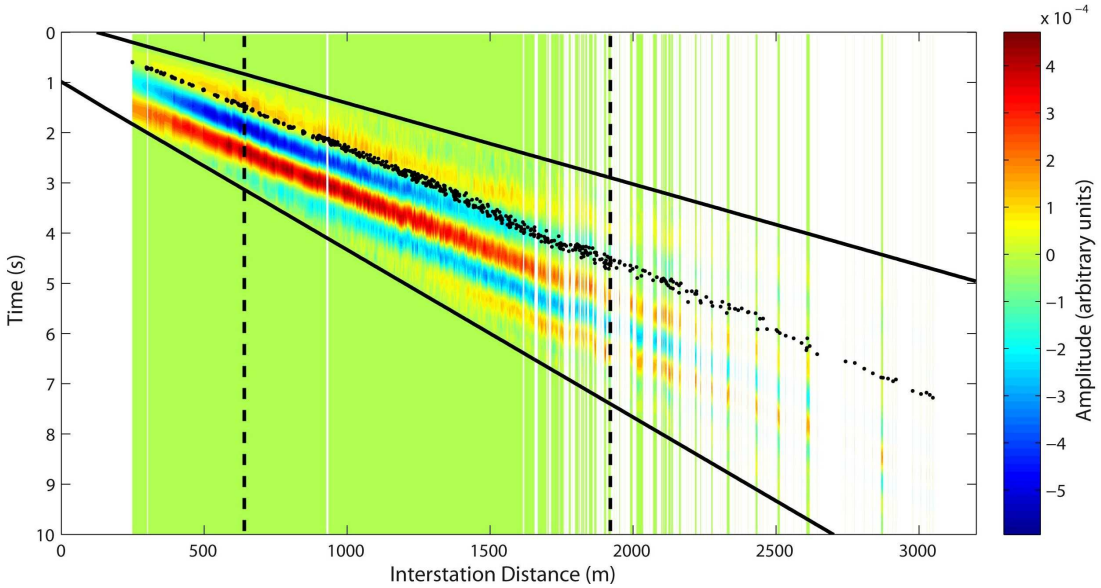

Figure 2

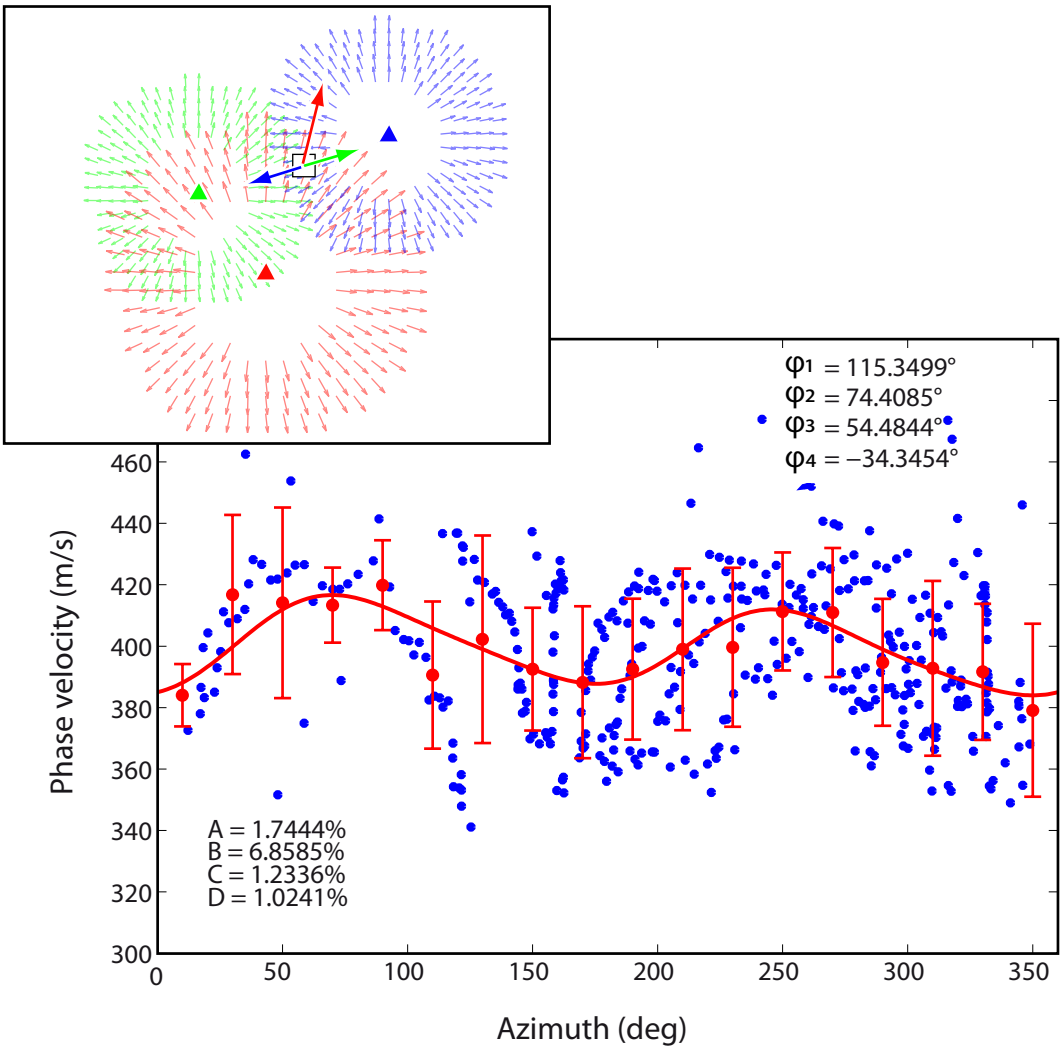
φ1 = 115.3499°
φ2 = 74.4085°
φ3 = 54.4844°
φ4 = −34.3454°
A = 1.7444%
B = 6.8585%
C = 1.2336%
D = 1.0241%
Phase velocity (m/s)
Azimuth (deg)
300
320
340
360
380
400
420
440
460
0
50
100
150
200
250
300
350

Figure 3

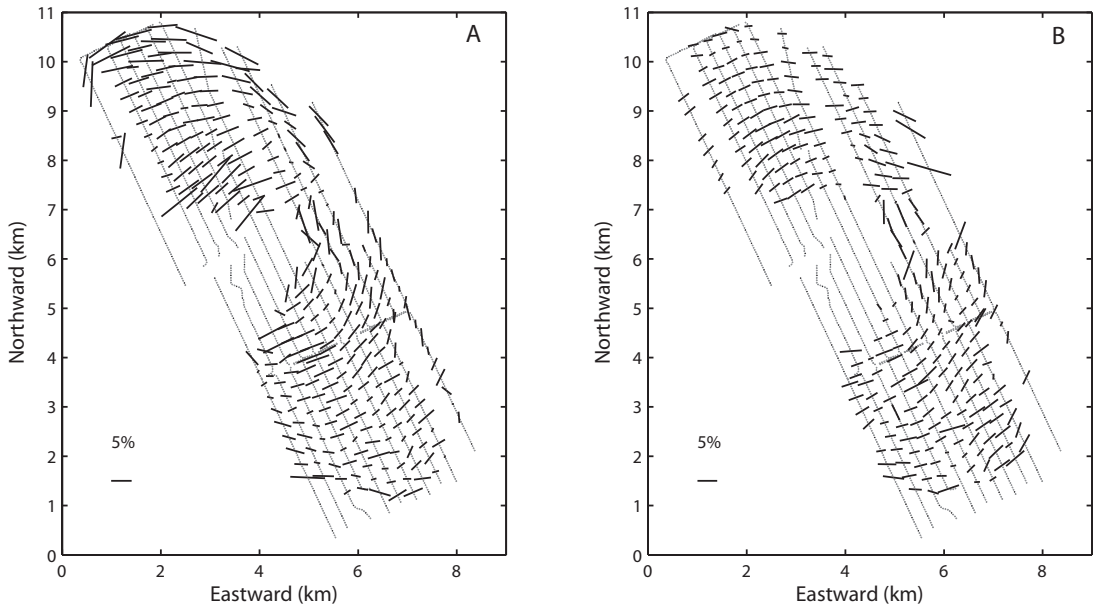

Figure 4

Supplementary materials

Figure S1: Schematic representation of the phase velocity computation (at station 595). A) The discrete travel times are spatially located at their corresponding stations. B) The travel times are interpolated onto a 50 m $\times$ 50 m regular grid and the travel time surface is cropped at the distances where the measurements become too sparse. C) The spatial gradient of the travel time surface is computed to give an estimate of the local phase slowness. D) The discrete amplitude data are interpolated onto the same grid than the travel times and the Laplacian-of-the-amplitude term of eq. 1 is computed and removed from the gradient term to give E) the distribution of local phase velocity as the magnitude of the vectors and F) the distribution of the local direction of wave propagation (black arrows, only every 5th arrows are shown for the clarity of the figure) as the direction of the vectors. The background color of frame F) shows the difference between the local direction of wave propagation and the straight ray approximation between the central station and each point of the grid.

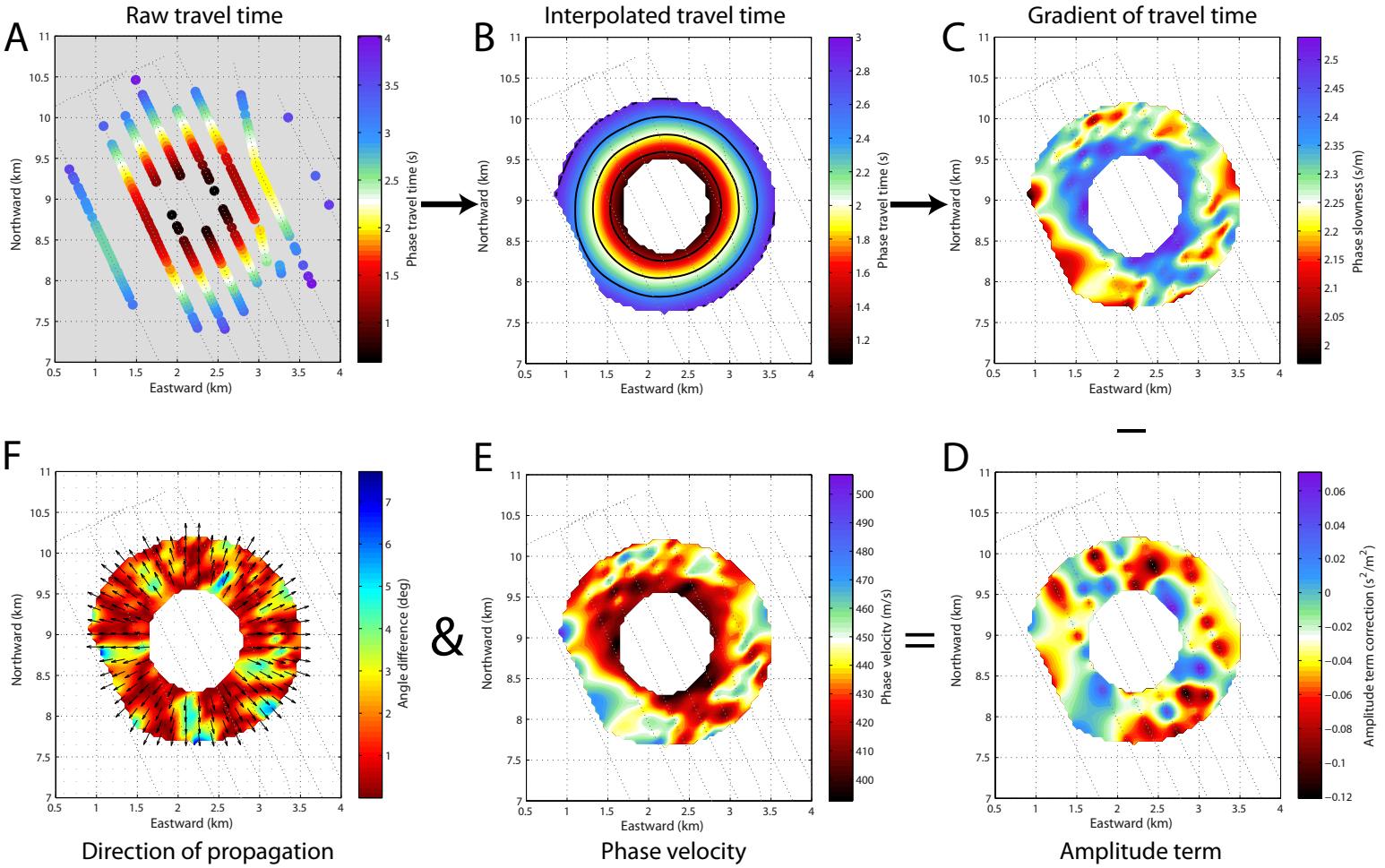
A
Raw travel time
B
Interpolated travel time
C
Gradient of travel time
Northward (km)
Eastward (km)
Phase travel time (s)
Phase slowness (s/m)
F
E
D
&
=
Angle difference (deg)
Phase velocity (m/s)
Amplitude term correction (s²/m²)
Direction of propagation
Phase velocity
Amplitude term

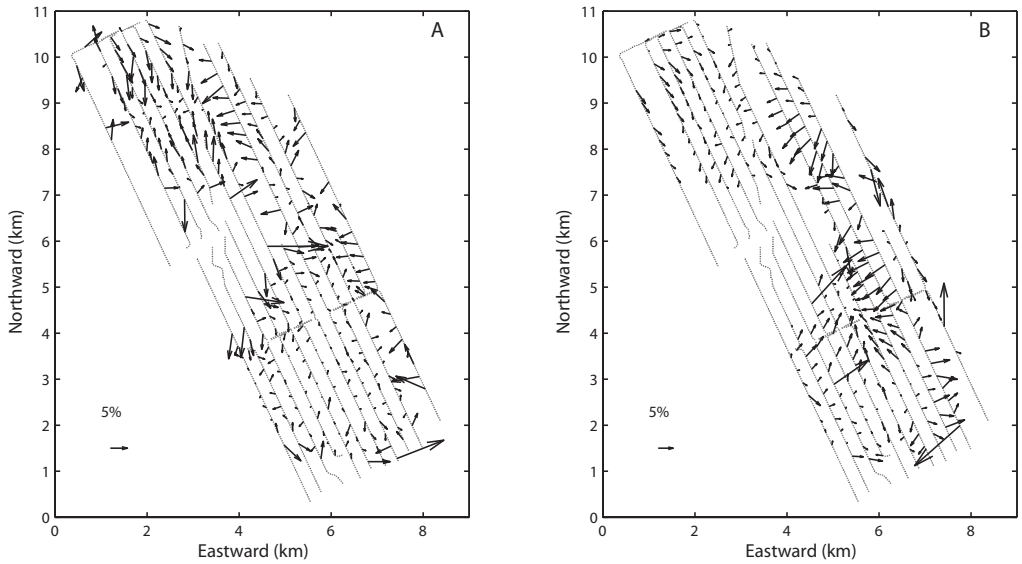

Figure S2: A) 1ψ azimuthal anisotropy fast direction and amplitude map at 0.7 s measured with the Helmholtz equation. B) 1ψ azimuthal anisotropy fast direction and amplitude map at 0.7 s measured with average phase velocities.

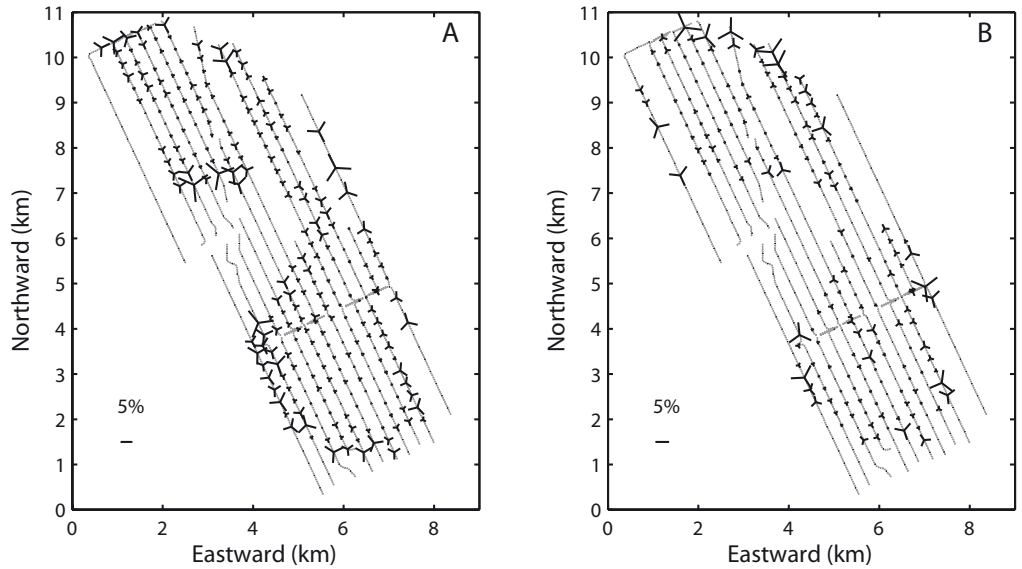

Figure S3: A) 3ψ azimuthal anisotropy fast direction and amplitude map at 0.7 s measured with the Helmholtz equation. B) 3ψ azimuthal anisotropy fast direction and amplitude map at 0.7 s measured with average phase velocities.

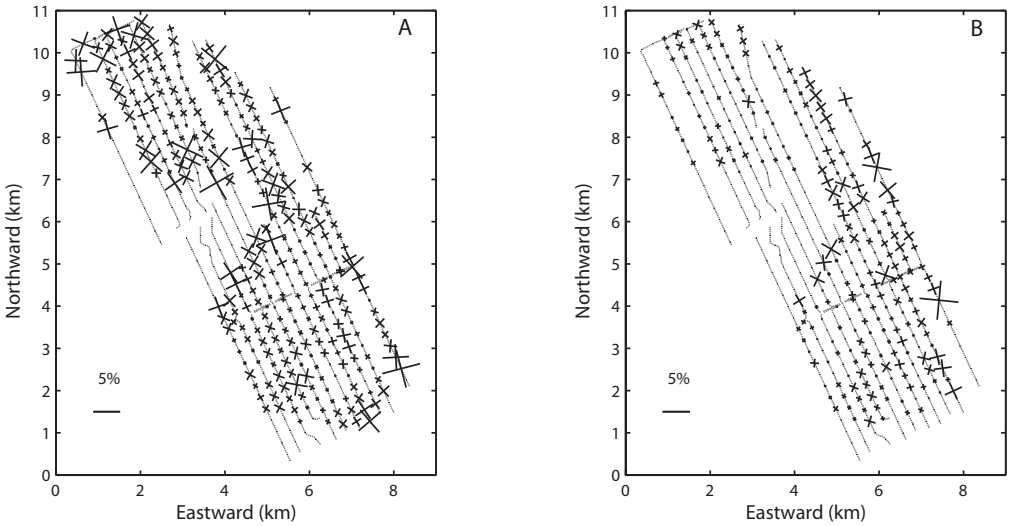

Figure S4: A) 4ψ azimuthal anisotropy fast direction and amplitude map at 0.7 s measured with the Helmholtz equation. B) 4ψ azimuthal anisotropy fast direction and amplitude map at 0.7 s measured with average phase velocities.

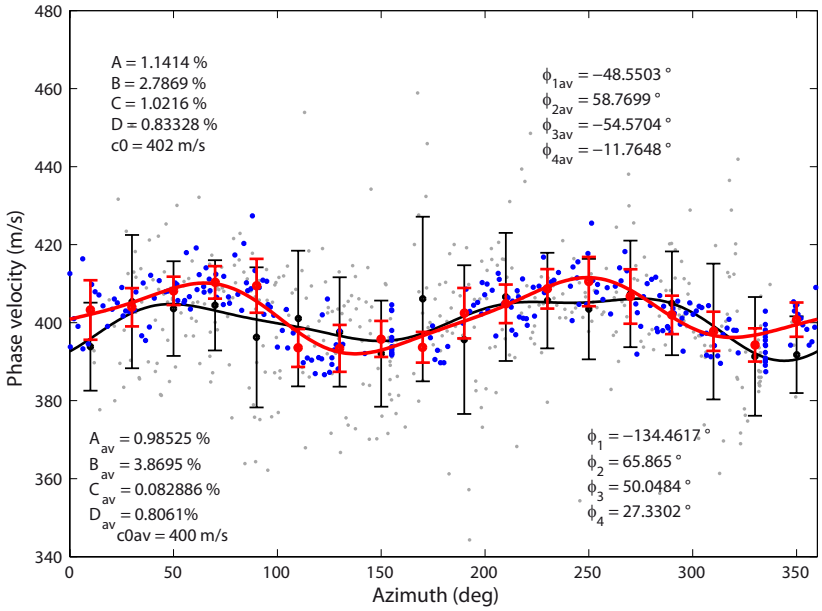

Figure S5: Azimuthal distribution of the phase velocity at 0.7 s for the station 1390 measured with average phase velocities. The small blue dots are the average phase velocity measurements. The large red dots with error bars are the average phase velocity averaged over 20°. The thick red curve is the best fits for the mean velocity, 1ψ, 2ψ,3ψ and 4ψ azimuthal parameters for the averaged velocity measurements. The values of the fitted parameters are shown with the subscript 'av'. For comparison, the gray dots show the Helmholtz tomography measurements, the black dots with error bars are the Helmholtz measurements averaged in 20° bins and the black curve is the best fit for the mean velocity, 1ψ, 2ψ,3ψ and 4ψ azimuthal parameters. The values of the fitted parameters are shown. Note that the phase velocity measurements are less scattered than for the Helmholtz approach. For the average phase velocity method, we need to solve for the initial phase ambiguity. To remove it, we force the linear regression of the measured travel-times vs inter-station distance to pass by the origin point (Distance, time) = (0,0) by removing the y-intercept value.

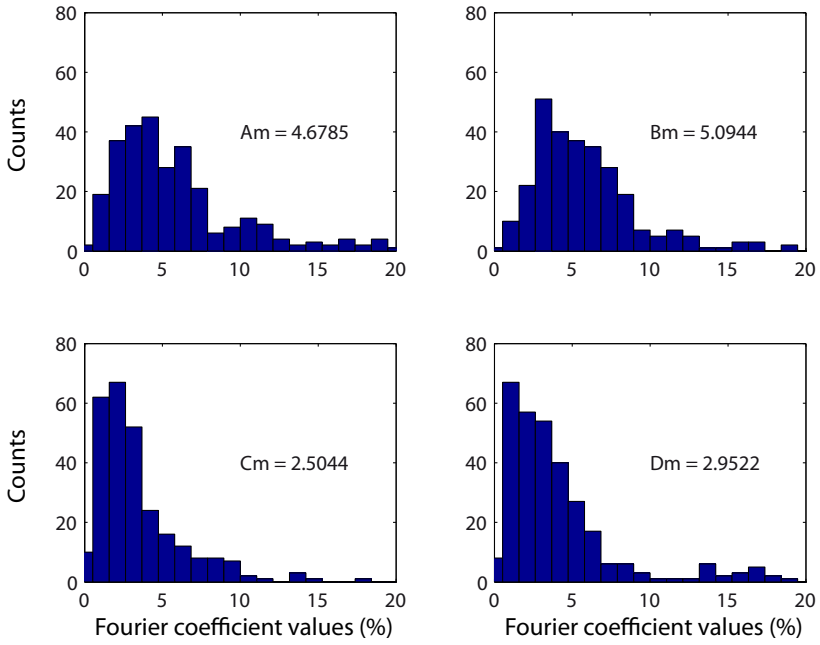

Figure S6: Distributions of the A, B, C and D parameters (in percent). The number in each frame is the median value of each parameter (note that the C and D values are in average about twice smaller than the A and B parameters).